AGU PUBLICATIONS

JGR

Journal of Geophysical Research: Oceans

RESEARCH ARTICLE

10.1002/2016JC012077

Gulf Stream variability and a triggering mechanism of its large meander in the South Atlantic Bight

Xiangming Zeng[1] and Ruoying He[1]

[1]Department of Marine, Earth, and Atmospheric Sciences, North Carolina State University, Raleigh, North Carolina, USA

Key Points:
- Weakly and strongly deflected patterns of the Gulf Stream in the South Atlantic Bight were confirmed by Self-Organizing Map analysis of satellite observations
- Interaction of transport increase and local bathymetry triggered the large Gulf Stream meander in November 2009 by conserving the potential vorticity
- Quantitative vorticity budget analysis further confirms this finding

Correspondence to:
R. He,
rhe@ncsu.edu

Citation:
Zeng, X., and R. He (2016), Gulf Stream variability and a triggering mechanism of its large meander in the South Atlantic Bight, *J. Geophys. Res. Oceans*, *121*, doi:10.1002/2016JC012077.

Received 21 JUN 2016
Accepted 11 OCT 2016
Accepted article online 13 OCT 2016

Abstract The Gulf Stream (GS) variability has an important impact on coastal circulation, shelf ecosystem, and regional weather and climate systems. Here we focus on the variability of the GS south of Cape Hatteras in the South Atlantic Bight (SAB). Statistical analysis on the 21 year satellite altimetry data reveals that the GS path in the SAB has two patterns: weakly and strongly deflected. The strongly deflected pattern is more likely to occur in winter. Over the last two decades, the largest GS offshore meander occurred in November 2009 to April 2010. Realistic ocean hindcast simulation and adjoint sensitivity analysis are used to investigate the triggering mechanisms for this extreme event. Our analyses show that a net increase of relative vorticity near the Charleston Bump was generated by strong interaction between increased GS velocity and local bathymetry, pushing the GS further offshore by virtue of conserving the potential vorticity. Quantitative vorticity analysis confirms this finding.

1. Introduction

Originating near the equator, the North Atlantic Ocean's Western Boundary Current (WBC) flows into the Caribbean Sea, forms the Caribbean Current, which subsequently becomes the Loop Current once it enters the Gulf of Mexico. Further downstream, the flow passes through the Florida Straits, becomes the Gulf Stream (GS), which moves through the South Atlantic Bight (SAB) and veers east into the open ocean off Cape Hatteras (Figure 1). Through this pathway, this WBC carries an enormous amount of volume and heat poleward, and plays a vital role in affecting both regional and global climate systems [*Schmeits and Dijkstra*, 2001; *Frankignoul et al*., 2001; *Kwon et al*., 2010].

While compared to other surface current systems, the WBC has a relatively stable main path, transport and speed, significant variability, and instabilities do exist [e.g., *Bane and Dewar*, 1988; *Liu and Gan*, 2012]. *Joyce and Zhang* [2010] and *Sanchez-Franks and Zhang* [2015] found that the variability of the GS path is linked to the strength of the Atlantic Meridional Overturning Circulation (AMOC). Focusing on a region downstream of the GS separation point (Cape Hatteras), they suggested that a more southerly (northerly) GS path occurs when the AMOC is relatively strong (weak). *Pérez-Hernández and Joyce* [2014] performed an analysis of two decades of satellite altimetry data in the similar deep-ocean region. The results revealed the bimodality of GS path variation and found that the GS shifts between 2010 and 2012 are the largest of last decade. More recently, several studies reported an extreme (∼30%) decline of the AMOC strength in 2009–2010 based on 10 years' (2004–2013) RAPID mooring observation [*Ezer*, 2015; *Goddard et al*., 2015; *Srokosz and Bryden*, 2015]. Because of the linkage between AMOC strength and GS position, the large shifts of GS path in 2010–2012 may be related to the extreme decline of AMOC strength in 2009–2010.

It is known that the cross-shelf position of the GS also has a large impact on coastal circulation, shelf ecosystem, and regional weather systems. For instance, earlier studies [e.g., *Bane and Dewar*, 1988; *Pérez-Hernández and Joyce*, 2014; *Gula et al*., 2015] have shown that strong meanders and eddies are common features of the GS in the SAB and the variability of the GS position grows with the increasing water transport from the Florida Straits to open ocean [*Schmitz and McCartney*, 1993]. Because the GS consists of high-temperature water, variations in GS position can affect sea surface temperature distribution, which moderates air-sea heat and moisture fluxes [*Minobe et al*., 2010], especially in winter [*Bane and Osgood*, 1989; *Li et al*., 2002; *Joyce et al*., 2009; *Nelson and He*, 2012; *Nelson et al*., 2014]. Frontal eddies and water intrusion resulted from variations in the GS position can enhance water exchange, shelf break upwelling, and deep-ocean nutrient delivery onto the shelf [*Miller and Lee*, 1995; *Castelao*, 2011], thereby influencing shelf-wide

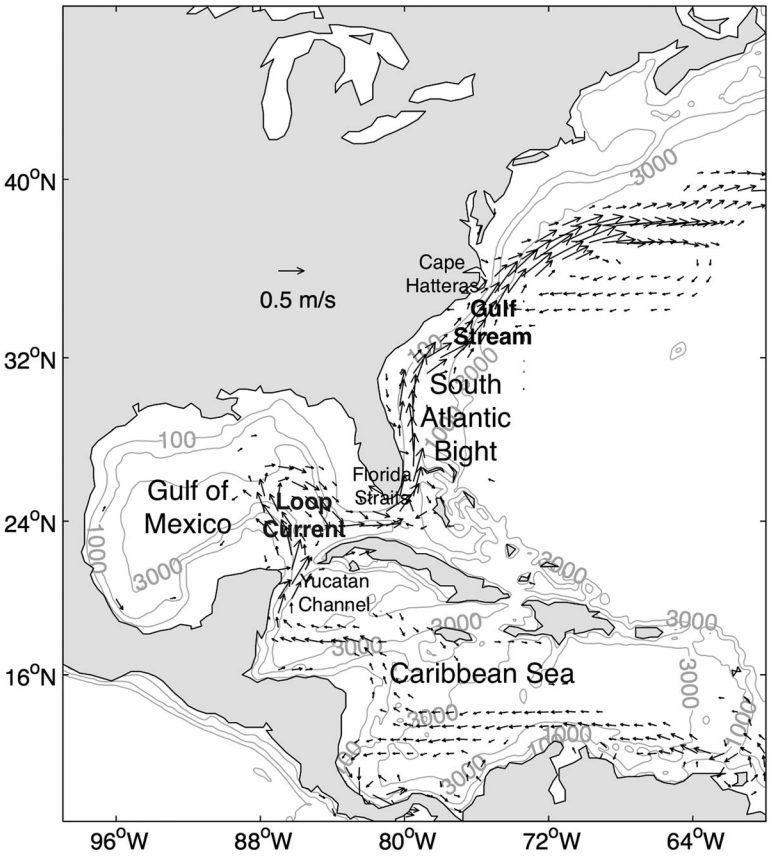

Figure 1. Model domain. Black arrows are geostrophic currents (>0.1 m/s) derived from 21 years of mean AVISO Absolute Dynamic Topography data. They can be considered as the Western Boundary Current system in the North Atlantic. Contours are 100, 1000, and 3000 m isobaths.

productivity and biomass [*Lee et al*., 1991; *Signorini and McClain*, 2007] as well as larval dispersal and distribution of fish populations [*Werner et al*., 1997; *Epifanio and Garvine*, 2001].

GS meanders along the continental margin in the SAB have been a long-standing research topic studied for decades. The first detailed observation was reported by *Webster* [1961], using measurements of surface salinity and velocity and water temperature in the top 200 m. Based on current meters and satellite imagery, *Bane and Dewar* [1988] suggested the seaward deflection of the GS near the Charleston Bump (Figure 2), a topographic feature located on the continental slope at 31.5°N offshore of Charleston, South Carolina, has a bimodal character of weakly and strongly deflected, and the transition between the two patterns occurs on an intermonthly time scale. *Miller* [1994] further supported this idea by analyzing 12 years of weekly GS position estimates and found a strong phase relationship between upstream water transport through the Florida Straits and the first principal component of GS position fluctuations. Furthermore, *Schmeits and Dijkstra* [2001] reasoned that the bimodal behavior of the GS is dynamically possible based on the dynamical system theory. By analyzing the energetics of numerical simulations, *Miller and Lee* [1995] concluded that the development of GS meanders and frontal eddies is controlled by a mixture of both baroclinic and barotropic instabilities of the mean flow. *Xie et al*. [2007] by using numerical sensitivity simulations with idealized topography showed that GS meanders are the results of combined effect of isobathic curvature of SAB bathymetry and the Charleston Bump. More recently, *Gula et al*. [2015] quantified the role played by interactions of the GS with topographic features and the subsequent impact of nonlinear eddy-mean flow interactions through a high-resolution model.

In this study, we examine the variability of the GS in the SAB and its dynamics using long-term satellite observations, new analysis, and numerical modeling methods. In section 2, we quantify the variation of the GS path in the SAB using two decades of satellite altimetry data and describe the large GS deflection

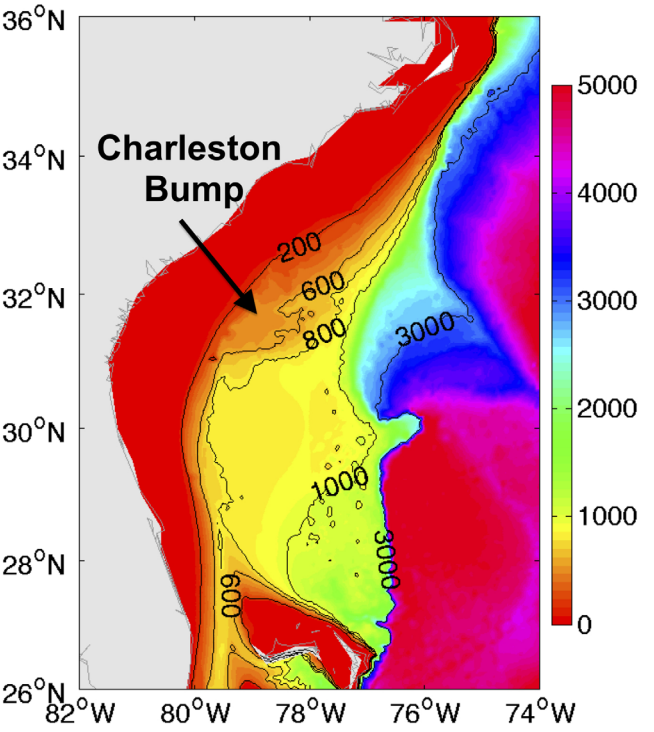

Figure 2. Topography of the South Atlantic Bight. Water depth is shown in meters and extracted from the 1 minute GEBCO data set. The Charleston Bump is indicated.

identified in November 2009 to April 2010. In section 3, we explore the trigging mechanism for this event using realistic numerical models and adjoint sensitivity analysis. Detailed flow field vorticity budget analysis is provided in section 4, followed with a conclusion and summary in section 5.

2. Gulf Stream Path Variation Over the Last Two Decades

2.1. Gulf Stream Path Detection

Different methods have been used in the past to track the GS path including the use of 15°C isotherm at 200 m [*Joyce et al.*, 2000] and maximum sea surface height (SSH) gradient [*Frankignoul et al.*, 2001; *Peña-Molino and Joyce*, 2008; *Lillibridge and Mariano*, 2013]. In this study, we applied the Canny edge detection method [*Canny*, 1986] on the 21 year AVISO gridded Absolute Dynamic Topography (ADT) to identify the location of the maximum gradient of the GS. The altimeter ADT products were produced by Ssalto/Duacs and distributed by Aviso, with support from CNES (http://www.aviso.altimeter.fr/duacs/). The data are constructed with two simultaneously operating altimeters, one in a 10 day exact repeat orbit (Topex/Poseidon, followed by Jason-1 and presently by Jason-2) and the other in a 35 day exact repeat orbit (ERS-1 followed by ERS-2 and presently by Envisat) [*Chelton et al.*, 2011]. The data have 1/4° spatial and daily temporal resolutions [*SSALTO/DUACS User Handbook*, 2015]. For quality control, only data from areas with water depth greater than 100 m were chosen for path detection [e.g., *Yin et al.*, 2014; *Zeng et al.*, 2015a, 2015b].

The Canny edge detection method finds edges by looking for local maxima of the field gradient. The gradient is calculated using the derivative of a Gaussian filter. The method can automatically find two thresholds of gradient, to detect strong and weak edges, and includes the weak edges in the output only if they are connected to strong edges. This method is therefore more robust than other edge detection methods in detecting true edges [*Mujumdar and Kumar*, 2012]. In the SAB, a strong ADT frontal gradient usually exists along the GS boundary. The resulting 21 year ADT edge locations are interpreted as the GS paths in the study region.

Figure 3 shows mean ADT (color shading), the detected GS mean path (solid black curve), corresponding envelope (dashed cyan curves), and one standard deviation lines (dashed black curves) from 1993 to 2013. The envelope represents the farthest (closest) location that the GS reached the open ocean (shelf) over the study duration. The mean path generally follows the 0.4 m contours of the mean ADT, with low ADT shoreward of the GS and high ADT seaward. From the topographic point of view, the mean path generally follows the 600 m isobaths from 28°N to 34°N, where the continental shelf is wide. From 34°N to Cape Hatteras, the shelf width decreases gradually, and the GS mean path moves to about the 2000 m isobaths, then separates from the continental shelf and veers east into the open ocean. The standard deviation is smaller compared to the envelope, meaning that large shifts of GS path occur infrequently. Both the standard deviation and the envelope increase from the Florida Straits to downstream of Cape Hatteras, especially around and downstream of the Charleston Bump.

To further quantify the variation of the Gulf Stream path, we calculated the GS offshore distance along five transects perpendicular to the mean path (Figure 3). Figure 4 show the GS position anomalies relative to the mean from 1993 to 2013. It is of interest to note that over the two decades, the largest Gulf Stream meander

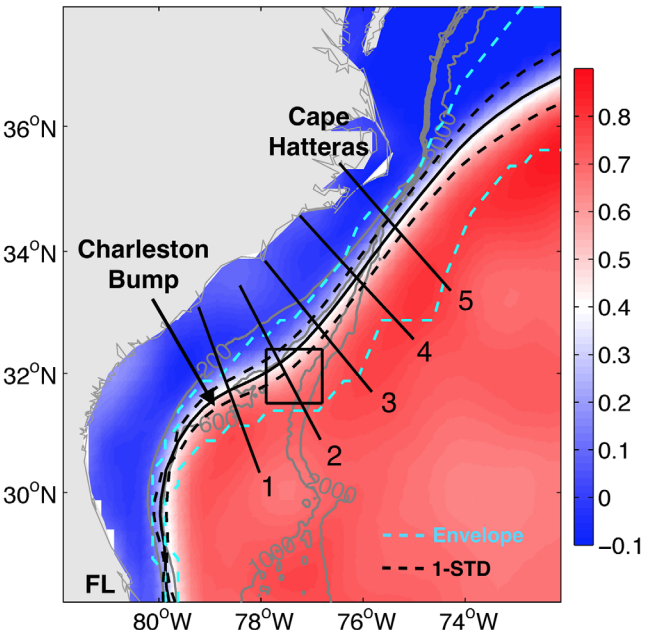

Figure 3. Long-term (1993–2013) mean Absolute Dynamic Topography (ADT, color shading, unit: m) overlaid with Gulf Stream mean path (solid black curve) and corresponding envelope (dashed cyan curves) and one standard deviation (STD, dashed black curves). Transects 1–5 (solid lines perpendicular to the Gulf Stream mean path) were used to measure the position variation of the Gulf Stream. Gray contours are 200, 600, 1000, and 2000 m isobaths. Black box is for the index function definition in section 3. Florida (FL) and the Charleston Bump are indicated.

occurred in November 2009 to April 2010. The offshore distance relative to its mean position increased from about 30 km at transect 1 to 90 km at transect 5.

2.2. Self-Organizing Map Analysis

With the derived GS location information, we also used the Self-Organizing Map (SOM) to cluster the GS paths in the SAB over the last 21 years.

The SOM is an effective method for feature extraction and classification. It is based on an unsupervised neural network and can map high-dimensional input data onto the elements of a regular, low-dimensional array [*Kohonen*, 2001]. It has been demonstrated to be more powerful than the conventional empirical orthogonal function method for feature extractions, especially when the signal is highly nonlinear [*Reusch et al.*, 2007; *Liu et al.*, 2006a]. The SOM is a mature method, and has been applied to identify patterns in ocean currents and sea surface temperature fields on the West Florida Shelf [*Liu and Weisberg*, 2005; *Liu et al.*, 2006b,2007], biogeochemical properties in the northern Adriatic Sea [*Solidoro et al.*, 2007], current variability in the China Seas [*Liu et al.*, 2008; *Jin et al.*, 2010; *Tsui and Wu*, 2012; *Yin et al.*, 2014], and SSH fields in the Gulf of Mexico [*Zeng et al.*, 2015a].

The SOM analysis identified two patterns of the GS paths in the SAB (Figure 5a). Pattern 1 is located very close to the GS mean position, whereas Pattern 2 is further offshore between 31.5°N and 34°N. This result is consistent with earlier finding about the GS bimodal behavior in the SAB [*Bane and Dewar*, 1988; *Miller*, 1994; *Schmeits and Dijkstra*, 2001]. Following the nomenclature used in *Bane and Dewar* [1988], we name Pattern 1 as the "weakly deflected" (red) pattern (P1) and Pattern 2 the "strongly deflected" (blue) pattern (P2).

To quantify the occurrence percentage of each pattern, the frequency of occurrence (FO) was calculated by summing the number of occurrences of each pattern divided by the total record length. Over two decades, the FO of the weakly deflected pattern was 74.1%, and the FO of the strongly deflected pattern was 25.9%. The latter smaller FO suggests the strong deflection (P2) is less frequent. Figure 5b shows the long-term monthly mean FO for each of the two patterns. As expected, the monthly FO of the strongly defected pattern (P2) was about 1/3 of the FO of the weakly deflected pattern (P1) in all months. Both patterns show weak seasonality. The strongly deflected pattern (P2) has a higher monthly FO in winter and lower monthly FO in summer, opposite that of the weakly deflected pattern (P1). In other words, the GS offshore meanders are more likely to occur in winter than in summer.

To explore possible relationship between Florida Current (FC) transport and the GS offshore meanders, we obtained the daily transport time series (www.aoml.noaa.gov/phod/floridacurrent/) measured at the Florida Strait at about 26.5°N. Daily values of FC transport are available from 1982 to 1998 and 2000 to present, so we chose the same time periods when both FC transport measurements and ADT data were available to make the correlation calculation. At the monthly scale, the FO of P2 is generally negatively correlated ($r = -0.81$) to FC transport (Figure 6a) and positively correlated with the monthly standard deviation (STD) of FC transport (Figure 6b). This interesting statistical result suggests that in winter (summer) months, the FC transport is lower (higher) with larger (smaller) STD, the corresponding FO of P2 is larger (smaller), thus the strongly deflected pattern is more (less) likely to occur. Influence of local wind forcing was also analyzed (not shown), but no significant relationship was found.

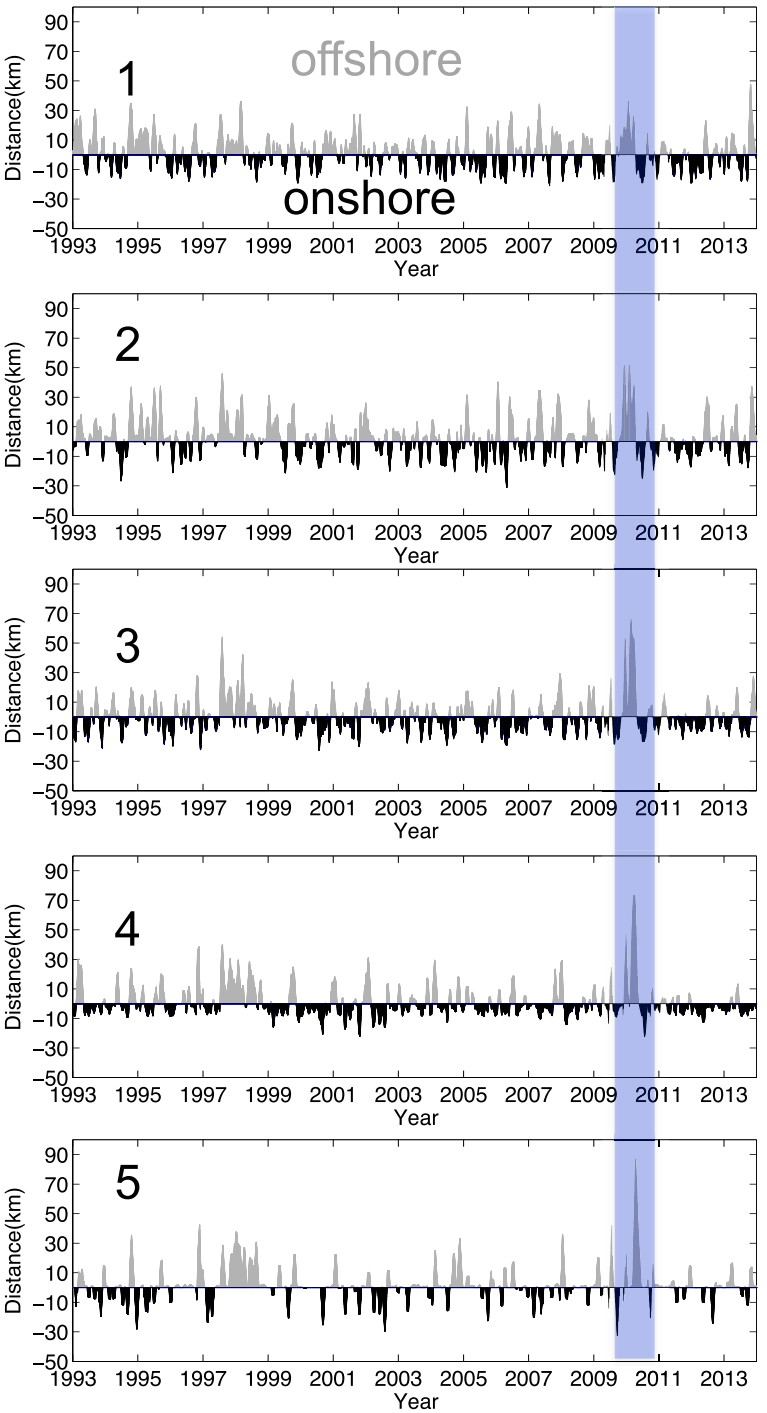

Figure 4. Gulf Stream position relative to its mean path along each transect in Figure 3 (unit: km). Offshore direction is positive (gray), while onshore is negative (black). Blue shaded region indicates the largest offshore event in 2009–2010. A 30 day low-pass filter was applied to the original data for visualization purpose.

3. Triggering Mechanism Analysis

Having discussed the long-term mean GS deflection patterns and their potential relationship with the Florida Current transport, we now switch the focus to the triggering mechanism for the extreme GS offshore deflection event that started in November 2009. The synoptic ocean state is the focus here, and we developed a realistic regional ocean hindcast model and its adjoint sensitivity tool for this analysis.

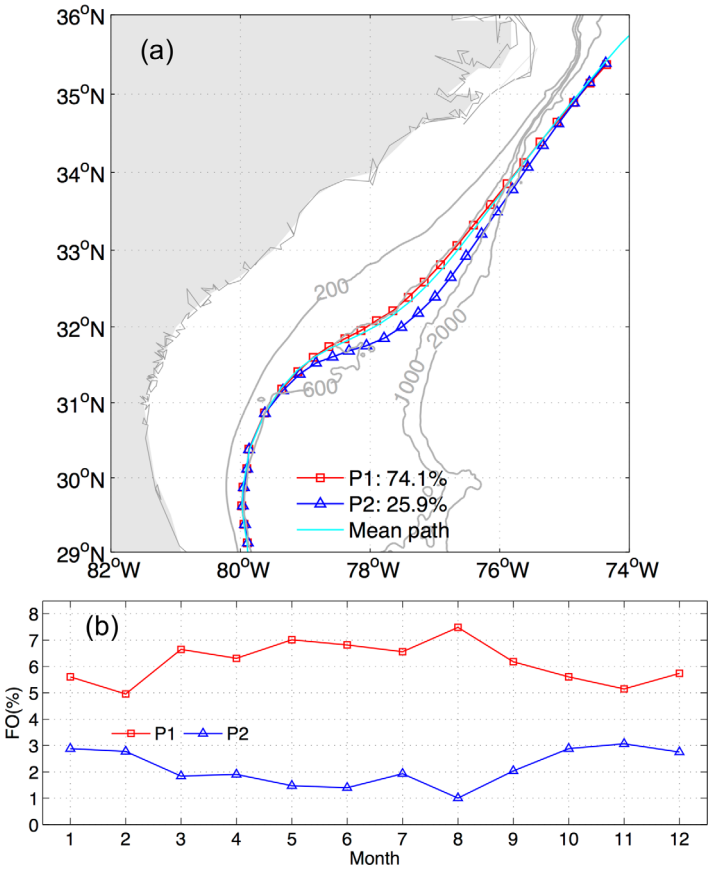

Figure 5. Self-Organizing Map analysis of the Gulf Stream path in the South Atlantic Bight. (a) Weakly (P1) and strongly (P2) deflected patterns. The numbers are corresponding frequency of occurrence (FO) for each pattern. The mean path is indicated by the cyan curve. (b) Monthly FOs of the two patterns in Figure 5a.

3.1. Ocean Model Configuration and Validation

We applied the Regional Ocean Modeling System (ROMS), specifically, its nonlinear forward model and its tangent-linear adjoint module for this analysis. ROMS is terrain-following coordinate, primitive equation model developed specifically for regional applications [*Haidvogel et al.*, 2008]. Its computational kernel uses high-order time stepping and advection schemes, and a carefully designed temporal averaging filter to guarantee exact conservation for tracers and momentum [*Shchepetkin and McWilliams*, 2005; *Zhang et al.*, 2009].

The model domain shown in Figure 1 spans the whole northwest Atlantic with ~7 km horizontal grid spacing and 36 vertical layers. The bathymetry is generated using 1 min gridded GEBCO data and smoothed with a linear programming procedure [*Sikirić et al.*, 2009] to remove overly large gradients that may lead to unwanted numerical pressure gradient errors for the model. The model uses fourth-order centered advection with the generic length scale vertical mixing scheme [*Warner et al.*, 2005] using k-kl mixing coefficients (corresponding to Mellor-Yamada Level 2.5).

At its only open boundary on the east, the model is configured to conserve volume with a free-surface Chapman condition, a Flather condition for the 2-D momentum, and clamped conditions for the 3-D momentum and tracers [*Marchesiello et al.*, 2001; *Powell et al.*, 2008; *Broquet et al.*, 2009; *Moore et al.*, 2009]. Boundary values of ocean states are derived from the daily global HYCOM/NCODA product (https://hycom.org).

Surface forcing used in the ROMS simulation is derived from the European Center for Medium Range Weather Forecast (ECMWF) reanalysis product (http://apps.ecmwf.int/datasets/data/interim-full-daily) with 0.125° grid spacing every 3 h. Air temperature, surface pressure, humidity, wind speed and direction, shortwave and long-wave radiation, and precipitation from ECMWF are used to compute the ROMS surface momentum and buoyance forcing with the bulk flux formulation of *Fairall et al.* [1996].

The model is initialized with daily HYCOM data and ran from 1 to 30 November 2009, when the largest Gulf Stream offshore meander in the last two decades began to initiate. Because the initial state variables interpolated from the global HYCOM output are in dynamically quasi-balanced conditions, the required spin-up time (9 days in this study) is much shorter than a simulation that spins up from the rest. Model results starting on 10 November onward are used for model-data comparison and analysis.

To assess the model skill, numerous model-data comparisons were performed. Figure 7, for example, shows the observed (blue) and simulated (red) daily sea level (normalized considering the difference in reference sea levels used in the model simulation and observations) at three stations along the SAB and water transport through the Florida Strait. The correlation coefficients between observations and simulations are all

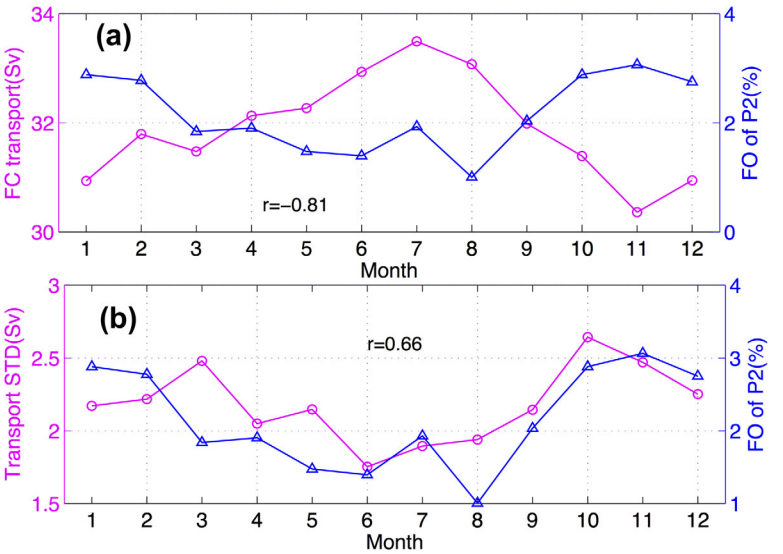

Figure 6. Comparisons between Florida Current (FC) transport and monthly FO of strongly deflected pattern (P2). (a) Monthly mean FC transport (Sv) and FO of P2 (%). Correlation coefficient is −0.81. (b) Monthly standard deviation (STD) of FC transport (Sv) and FO of P2 (%). Correlation coefficient is 0.66.

greater than 0.86 and the magnitude of simulated water transport also generally matches with the observed. These suggest that the model realistically reproduces SAB circulation during this study period.

3.2. Adjoint Sensitivity Model

A unique tool we used in this study is the adjoint sensitivity analysis. Given the simulated ocean state, the adjoint model allows one to go backward in time to track factors that were important for triggering the large GS offshore meanders in November 2009. The adjoint model has been widely studied in meteorological and oceanographic communities [*Errico*, 1997; *Bennett*, 1992, 2002; *Wunsch*, 1996, 2006]. Recently, it has been developed and implemented into ocean models either for sensitivity studies or data assimilation purposes. *Marotzke et al.* [1999] described the construction of the adjoint MIT general circulation model with the automatic differentiation method. *Chua and Bennett* [2001] developed a system for variational assimilation of data into ocean models based on the adjoint method. Along with the tangent linear and adjoint components, the data assimilation system of the Regional Ocean Modeling System (ROMS) has been described in a series of papers [*Moore et al.*, 2004, 2011a, 2011b, 2011c]. Several studies have applied adjoint sensitivity to study ocean processes, such as the sensitivity studies of the Kuroshio Current [*Ishikawa et al.*, 2004], meridional overturning circulation [*Bugnion et al.*, 2006], the California Current [*Moore et al.*, 2009; *Veneziani et al.*, 2009], New York Bight circulation [*Zhang et al.*, 2009], and the Loop Current in the Gulf of Mexico [*Gopalakrishnan et al.*, 2013].

The basic ideas of the adjoint model are the first-order Taylor approximation and Lagrange multiplier method. Following *Moore et al.* [2004] and *Zhang et al.* [2009], we consider the nonlinear ocean model (NLM), also known as the forward model:

$$\begin{cases} \dfrac{\partial \mathbf{\Phi}(\mathrm{t})}{\partial \mathrm{t}} = M(\mathbf{\Phi}(\mathrm{t})) + \mathbf{F}(\mathrm{t}) \\ \mathbf{\Phi}(0) = \mathbf{\Phi}_0 \\ \mathbf{\Phi}(\mathrm{t})|_{\Omega} = \mathbf{\Phi}_{\Omega}(\mathrm{t}) \end{cases} \tag{1}$$

where $\mathbf{\Phi}(\mathrm{t})$ is a state vector of $(u,\ v,\ T,\ S,\ \eta)$ representing the west-east velocity, south-north velocity, temperature, salinity, and sea level of all model grids at time t; M is the nonlinear operator of the model; $\mathbf{F}(\mathrm{t})$ is the external forcing at time t; $\mathbf{\Phi}_0$ are the initial conditions; $\mathbf{\Phi}_{\Omega}(\mathrm{t})$ are the boundary conditions along boundary Ω. Suppose $\mathbf{\Phi}_c$ is a certain solution of equation (1), and we introduce small perturbations $\phi_0 = \delta\mathbf{\Phi}_0$, $\phi_{\Omega}(t) = \delta\mathbf{\Phi}_{\Omega}(\mathrm{t})$, and $\mathbf{f}(t) = \delta\mathbf{F}(\mathrm{t})$ to the initial conditions, boundary conditions, and external forcing, respectively. The corresponding perturbations of the solution $\mathbf{\Phi}_c$ can be expressed as $\phi = \mathbf{\Phi} - \mathbf{\Phi}_c$. Then, we can get the perturbation by considering the difference between original and perturbed equations:

$$\begin{cases} \dfrac{\partial \boldsymbol{\phi}(\mathrm{t})}{\partial \mathrm{t}} = M(\boldsymbol{\Phi}(\mathrm{t})) - M(\boldsymbol{\Phi}_{\boldsymbol{c}}(\mathrm{t})) + \mathbf{f}(\mathrm{t}) \\ \boldsymbol{\phi}(0) = \boldsymbol{\phi}_0 \\ \boldsymbol{\phi}(\mathrm{t})|_{\Omega} = \boldsymbol{\phi}_{\Omega}(\mathrm{t}) \end{cases} \tag{2}$$

Using the first-order Taylor approximation, we have

$$M(\boldsymbol{\Phi}(\mathrm{t})) = M(\boldsymbol{\Phi}_{\boldsymbol{c}}(\mathrm{t})) + \left.\frac{\partial M}{\partial \boldsymbol{\Phi}}\right|_{\boldsymbol{\Phi}_c} (\boldsymbol{\Phi} - \boldsymbol{\Phi}_c) \tag{3}$$

Plug equation (3) into equation (2) and considering $\boldsymbol{\phi} = \boldsymbol{\Phi} - \boldsymbol{\Phi}_c$, we have the tangent linear model (TLM):

$$\begin{cases} \dfrac{\partial \boldsymbol{\phi}(\mathrm{t})}{\partial \mathrm{t}} = \left.\dfrac{\partial M}{\partial \boldsymbol{\Phi}}\right|_{\boldsymbol{\Phi}_c} (\boldsymbol{\Phi} - \boldsymbol{\Phi}_{\boldsymbol{c}}) + \mathbf{f}(\mathrm{t}) = C\boldsymbol{\phi} + \mathbf{f}(\mathrm{t}) \\ \boldsymbol{\phi}(0) = \boldsymbol{\phi}_0 \\ \boldsymbol{\phi}(\mathrm{t})|_{\Omega} = \boldsymbol{\phi}_{\Omega}(\mathrm{t}) \end{cases} \tag{4}$$

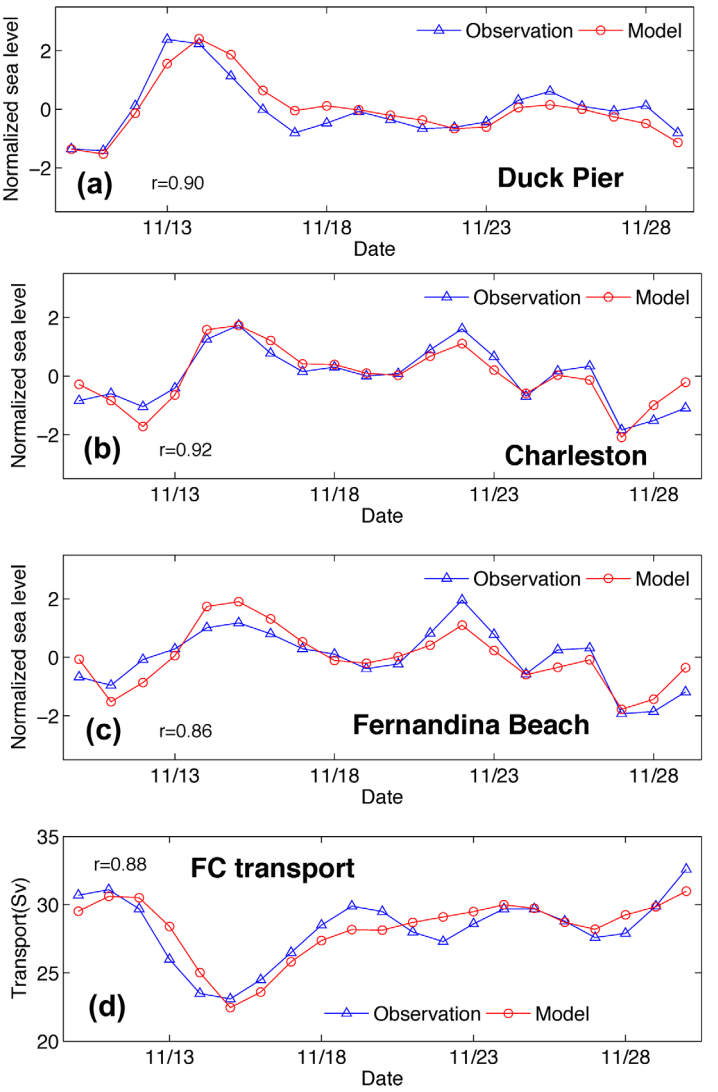

Figure 7. (a–c) Observed (blue) and simulated (red) daily sea level at three stations along the SAB, and (d) water transport through the Florida Straits. Sea level data are normalized (minus mean divided by the corresponding standard deviation). Locations of the three stations and the FC transect are shown in Figure 8a.

where C is the Jacobian matrix. After it is discretized in space and time, the TLM yields a system of linear equations [*Zhang et al.*, 2009]:

$$\mathbf{A}\boldsymbol{\phi} = \mathbf{b} \tag{5}$$

where **A** is the corresponding coefficient matrix, and **b** is a vector consisting of the perturbations of boundary conditions, initial conditions, and external forcing terms. That is, if we let vectors **r** and $\mathbf{r}_{\boldsymbol{c}}$ be the boundary conditions, initial conditions, and external forcing terms corresponding to the solution $\boldsymbol{\Phi}$ and $\boldsymbol{\Phi}_{\boldsymbol{c}}$, respectively, then $\mathbf{b} = \mathbf{r} - \mathbf{r}_{\boldsymbol{c}}$.

We can define an index scalar function $J(\boldsymbol{\Phi})$ to represent the model state we want to explore the sensitivity. Because $\boldsymbol{\phi} = \boldsymbol{\Phi} - \boldsymbol{\Phi}_c$, we have $J(\boldsymbol{\Phi}) = J(\boldsymbol{\phi} + \boldsymbol{\Phi}_c) = G(\boldsymbol{\phi})$. Applying the Lagrange multiplier method [*Bertsekas*, 1982] to the function $G(\boldsymbol{\phi})$, we get a cost function:

$$L = G(\boldsymbol{\phi}) + \boldsymbol{\lambda}^T(\mathbf{A}\boldsymbol{\phi} - \mathbf{b}) \tag{6}$$

where $\boldsymbol{\lambda}$ is the Lagrange multiplier vector, and T represents transpose. Note that L has the same minimum as $G(\boldsymbol{\phi})$ subject to equation (5). Let $\mathbf{g}(\boldsymbol{\phi}) = \mathbf{A}\boldsymbol{\phi} - \mathbf{b}$. According to *Ito and Kunisch* [2008], we have

$$\frac{\partial G}{\partial \boldsymbol{\phi}} + \boldsymbol{\lambda}^T \frac{\partial \mathbf{g}}{\partial \boldsymbol{\phi}} = 0 \tag{7}$$

which can also be derived by setting $\frac{\partial L}{\partial \boldsymbol{\phi}} = 0$ [*Bennett*, 2002;

Zhang et al., 2009]. After taking the transpose of both sides of (7), and considering $\frac{\partial G}{\partial \phi} = \frac{\partial J}{\partial(\mathbf{\Phi}-\mathbf{\Phi}_c)} = \frac{\partial J}{\partial \mathbf{\Phi}'}$ we can get the adjoint model (ADM):

$$-\mathbf{A}^T\boldsymbol{\lambda} = \left(\frac{\partial J}{\partial \mathbf{\Phi}}\right)^T \tag{8}$$

$\boldsymbol{\lambda}$ can be considered a sensitivity measure of a certain ocean state J to initial conditions, boundary conditions, and external forcing fields $\mathbf{r}$. Considering $\mathbf{g}(\phi)=\mathbf{A}\phi-\mathbf{b}$, $\mathbf{b}=\mathbf{r}-\mathbf{r_c}$, $\phi=\mathbf{\Phi}-\mathbf{\Phi}_c$, and the chain rule, we have

$$\left(\frac{\partial J}{\partial \mathbf{r}}\right)^T = \left(\frac{\partial J}{\partial \mathbf{\Phi}}\frac{\partial \mathbf{\Phi}}{\partial \mathbf{r}}\right)^T = \left(\frac{\partial G}{\partial \phi}\frac{\partial \phi}{\partial \mathbf{r}}\right)^T = \left(-\boldsymbol{\lambda}^T\frac{\partial \mathbf{g}}{\partial \phi}\frac{\partial \phi}{\partial \mathbf{b}}\right)^T = -\left(\boldsymbol{\lambda}^T\frac{\partial \mathbf{g}}{\partial \mathbf{b}}\right)^T = -\left(-\boldsymbol{I}\boldsymbol{\lambda}^T\right)^T = \boldsymbol{\lambda} \tag{9}$$

where $\boldsymbol{I}$ is the identity matrix. The adjoint sensitivity can measure the real changes of certain ocean states due to the perturbation of certain factors such as velocity. However, the units of $\frac{\partial J}{\partial \mathbf{r}}$ vary across components, complicating the direct comparison of the sensitivities. Following *Moore et al*. [2009], we can consider the changes $\Delta J_i = \Delta \boldsymbol{r}_i \frac{\partial J}{\partial \boldsymbol{r}_i}$ that would result from perturbations $\Delta\mathbf{r}$ at each grid point i within the target region and time. Standard deviation of each element at grid point i is typically chosen as $\Delta \boldsymbol{r}_i$. Therefore, the direct comparison of ΔJ_i arising from perturbations in each component of $\mathbf{r}$ provides an immediate quantitative appreciation of the sensitivity of J to perturbations with amplitudes typical of those encountered in the real ocean. If J represents the mismatch between the NLM state and observations, minimizing J is one method of doing data assimilation. If J is a measure of some model state of NLM, the adjoint sensitivity identifies locations and variables that are important to this feature [*Zhang et al*., 2009].

3.3. Forward Model Results

Figure 8 shows the simulated surface velocity and relative vorticity (normalized by the Coriolis parameter) from 17 to 26 November 2009, in 3 day intervals. As shown by simulation, the GS speed is at a maximum along the continental shelf in this region. Due to the strong velocity shear along edges of the GS, positive relative vorticity occurs shoreward, and negative relative vorticity exists seaward. From the Florida Straits to the Charleston Bump, the GS path generally follows the 600 m isobaths. As the width of the continental shelf decreases, the GS moves further offshore to the 2000 m isobaths. From 17 to 26 November, a large meander developed downstream of the Charleston Bump, which moved the GS position (near the black box in Figure 8) further offshore. Numerous eddies (both anticyclones and cyclones) were present seaward of the GS, visible in both the velocity and relative vorticity fields.

As shown by the simulation (Figure 8), both the Florida Current (FC), which flows through the Florida Straits, and the Antilles Current (AC), which passes northeast of Abaco Island, Bahamas contribute to the formation of the GS. The validity of the AC remains questionable due to its discontinuous nature and weak dynamic signal [*Rowe et al*., 2013]. The hydrographic study of *Gunn and Watts* [1982] found that the AC acts more as an eddy field rather than as a continuous jet. *Lee et al*. [1996] concluded that the AC serves to balance the interior Sverdrup circulation not accounted for by the FC and that it is not a continuous flow along the Bahamas and Antilles island chain. In our study duration, however, we can see a clear flow path of the AC from Abaco Island to the SAB in the simulated surface velocity fields (Figures 8a–8c). Even though the surface path of the AC into the GS has less distinct surface structure on 26 November (Figure 8d), the AC beneath the surface consistently contributes to the GS (not shown). During the study time period, the AC appears to be strongly influenced by the presence of the anticyclonic eddy around 76°W, 27°N (Figure 8a). The AC transport during this period is likely to be enhanced by the presence of this eddy. The estimates of AC transport vary from different studies. *Lee et al*. [1996] presented a range from 2 to 7 Sv (net transport) with a mean northward flow of 5 $\pm$ 2 Sv at 27°N. In contrast, *Schmitz and McCartney* [1993] reported a much higher value of 12 Sv. Our simulated AC transport (Figure 9) shows a similar estimation to that of *Schmitz and McCartney* [1993]. Although we note that our transect for AC transport calculation is different from *Lee et al*.'s [1996], but similar to that of *Schmitz and McCartney* [1993].

The GS water transport calculated immediately upstream of the Charleston Bump (Figure 9) is ~40 Sv. Due to the adjustment of the AC on the continental shelf before joining the GS, not all AC water through the Abaco transect goes into the GS. The transport magnitude indicates that the FC is the major contributor of the GS in the SAB, which accounts for ~75% (~30 Sv) of water transport. That leaves ~25% (~10 Sv)

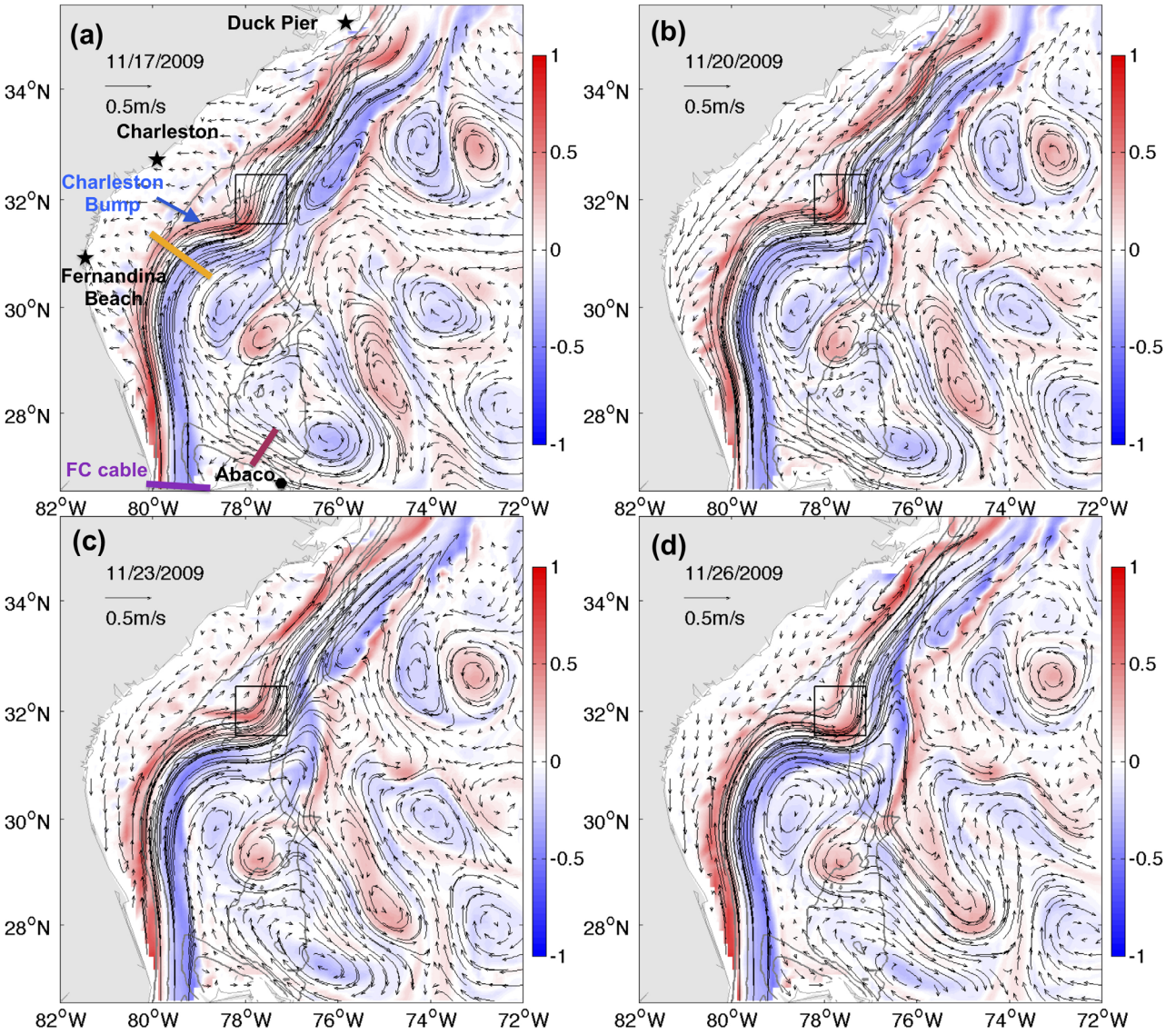

Figure 8. Simulated surface velocity (vectors) and relative vorticity (color shading) from 17 to 26 November 2009, every 3 days. Relative vorticity is normalized by dividing by the Coriolis parameter. Black stars in Figure 8a indicate the location of the three sea level stations, and black hexagon represents Abaco Island. Purple solid line in Figure 8a represents the location of the cable measuring the Florida Current (FC) transport. Black box (same as the one in Figure 3) delineates the region for index function calculation. Gray lines are the 200, 600, 1000, and 2000 m isobaths. The purple, red, and yellow transects in Figure 8a are sites where water transport was calculated for the FC, Antilles Current, and Gulf Stream, respectively.

coming from the AC. We calculated that ~67% of AC water goes into the GS, while ~23% recirculates to the deep ocean. These estimates are based on a 1 month simulation. Over a longer time scale, the results may differ.

Another interesting pattern as shown in Figure 9 is the sudden drop of water transport within 4 days at all three transects. For the GS, water transport drops ~5 Sv from 13 November, and reaches the lowest value in the study period on the 16 November. For the FC, the drop (~8 Sv) happens from 12 to 15 November. For the AC, the drop (~4 Sv) also occurs from 12 to 15 November. Because the FC speed (~1.5 m/s) is much greater than that of the AC (~0.3 m/s), the water transport signals at the Florida Straits and Abaco transects should propagate to the transect upstream of Charleston Bump at different times. Therefore, the ~5 Sv drop of GS water transport from 13 to 16 November approximately corresponds to the drop of FC transport (~8 Sv) from 12 to 15 November and the slight increase of AC transport before 12 November. In this way, the water transport values can generally be consistent. In the following section, we will show the influence of the sudden transport recovery following the sudden transport drop on the formation of large Gulf Stream offshore meanders.

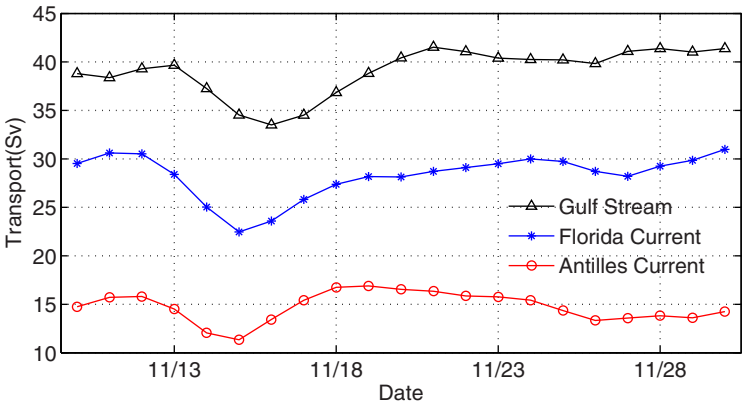

Figure 9. Simulated water transport through the three transects in Figure 8a. These indicate the water transport of Florida Current, Antilles Current, and Gulf Stream.

3.4. Validity of Tangent Linear Assumption and Index Function Definition

As noted in section 3.1, adjoint sensitivity analysis is based on the validity of the tangent linear assumption. Before performing adjoint sensitivity analysis, the validity of the tangent linearization should be verified. This is done by comparing fifty random perturbation runs with the corresponding TLM solutions.

From a 5 year forward simulation, we randomly select an ocean state perturbation (dx) relative to its mean, and set dx as the initial value for the TLM (g). Assuming x_0 is the initial field for the original forward model (f), we can then compare the difference of forward model ($f(x_0+dx,\ t)-f(x_0,\ t)$) with the TLM solutions ($g(dx,\ t)$), and choose the proper time scale indicated by the correlation coefficients. Fifty perturbation (i.e., SSH$\sim$0.2 m, velocity$\sim$0.4 m/s) runs are implemented with dynamically relevant amplitudes. As shown in Figure 10, correlation coefficients gradually decrease as the time window increases. The time scale of linearization for SSH is longer than that of velocity. We chose the time scale for valid tangent linear assumption to be 10 days, when the mean correlation coefficient of the velocity comparisons is around 0.6.

To use the adjoint model, an index function J (also called cost function or penalty function in other references) must be defined as a function of model output variables. Similar to *Gopalakrishnan et al*. [2013], we define the index function as the negative daily mean SSH in the black box of Figure 3 to represent the variation of GS position adjacent to transect 2 (Figure 3). That is,

$$J=-\frac{1}{(t_2-t_1)A}\int_{t_1}^{t_2}\int_A \eta dA\ dt \tag{10}$$

where η is SSH, A is the area, and the time range is t_1 to t_2 (1 day for this case).

The model simulation shows that the mean SSH within the black control box is very well inversely correlated with the GS position along transect 2 (Figure 11). That is, when the GS moves seaward, the SSH inside the control box decreases, and vice versa. The correlation coefficient of the two variables is highly significant ($r=-0.9$) during the study period, indicating the validity of choosing this index function to represent GS path variation.

Because the tangent linear assumption is valid for 10 days (shown above), a 10 day window from 17 to 26 November was selected for the adjoint sensitivity analysis (show by the dashed rectangle in Figure 11). During this time period, the GS moved seaward, while mean SSH within the control area decreased. Using the adjoint model, we can go backward in time and diagnose what processes triggered the GS offshore motion on 26 November.

3.5. Adjoint Sensitivity Analysis

Figure 12 shows the adjoint sensitivity of index function J to the depth-averaged velocity field $\left(\frac{\partial J}{\partial U},\frac{\partial J}{\partial V}\right)$ going backward in time from 26 to 17 November, every 3 days. Following *Moore et al*. [2009], the sensitivity is plotted as a velocity vector field. Physically, such an adjoint sensitivity can be considered as a scaled barotropic velocity perturbation [*Moore et al*., 2009], which caused the large GS seaward motion on 26 November 2009. On 26 November, the sensitivity area was around the index-defining black box (Figure 12a) in a form of a cyclonic velocity perturbation. This cyclonic perturbation is positive, indicating a positive relative vorticity perturbation is present at that time point. Going backward in time, the sensitivity region gradually extends to the north and south largely along the isobaths (Figure 12d). The cyclonic feature on 26 November can be further traced back to the cyclonic perturbation around the Charleston Bump on 17 November, which can be subsequently traced back to the Florida Strait. This is most evident in the northward sensitivity vector fields along

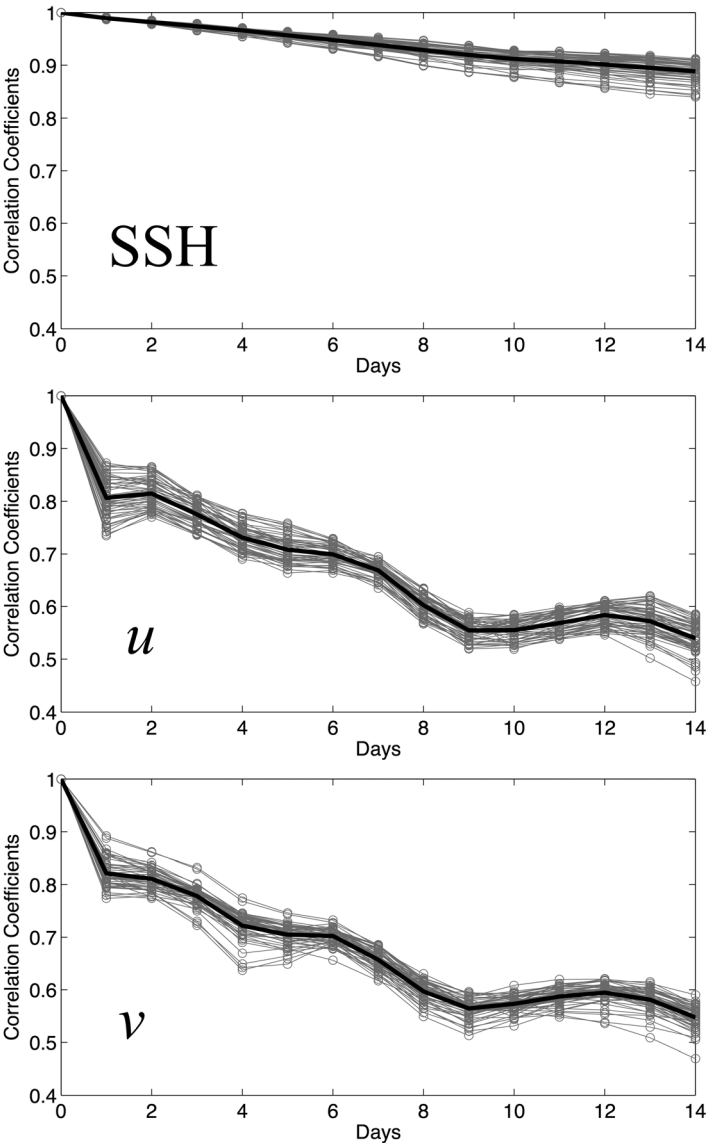

Figure 10. Comparisons between the nonlinear perturbation runs and tangent linear model solutions in terms of sea surface height (SSH) and velocity (*u* and *v*). Gray lines represent the 50 perturbation experiments, and solid black lines are the corresponding mean.

the GS main path, indicating a positive velocity perturbation (i.e., increase of GS velocity) that started from 15 November can lead to an increase of index function *J* (Figure 9) over the study period. Because the GS flows northward through the Florida Straits, the increase of water transport through the Florida Straits caused the GS velocity enhancement, thus a positive velocity perturbation reflected in the sensitivity field. This increased GS velocity interacts with the topographic feature near the Charleston Bump, producing a cyclonic vorticity perturbation in the area.

The sensitivity seaward of the 1000 m isobaths from 32°N to 36°N is also noticeable, suggesting a possible interaction of the GS with deep boundary currents or eddies may also contribute to the perturbation of *J*. Seaward of the 600 m isobaths from 27°N to 30°N, the decreasing velocity perturbation (indicated by the southward vector field) corresponds to the transport decline of the Antilles Current (AC) starting from 12 November 2009 (Figure 9). The sensitivity of index function *J* to the depth-averaged velocity field is relatively small in other regions (Figure 12d).

Figure 13 provides a conceptual schematic to illustrate how the increased velocity field interacts with the topography to cause the GS move seaward. Assume the normal state of the stream velocity field is largely symmetric due to velocity shear and balance (Figure 13a). Positive relative vorticity exists

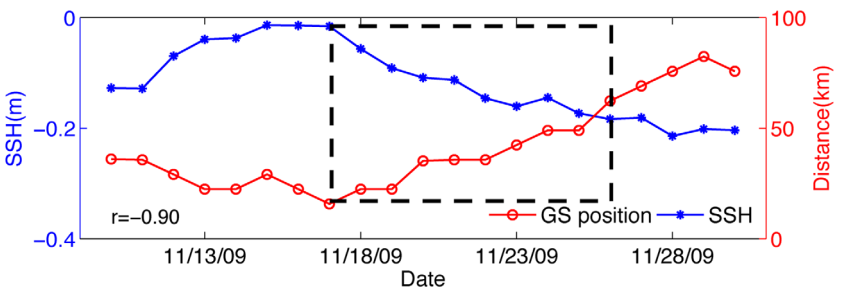

Figure 11. Comparison between daily mean sea surface height (SSH, blue) in the box and Gulf Stream (GS) position (red) relative to the mean path along transect 2 in Figure 3. The dashed rectangular box indicates the time window for adjoint sensitivity analysis.

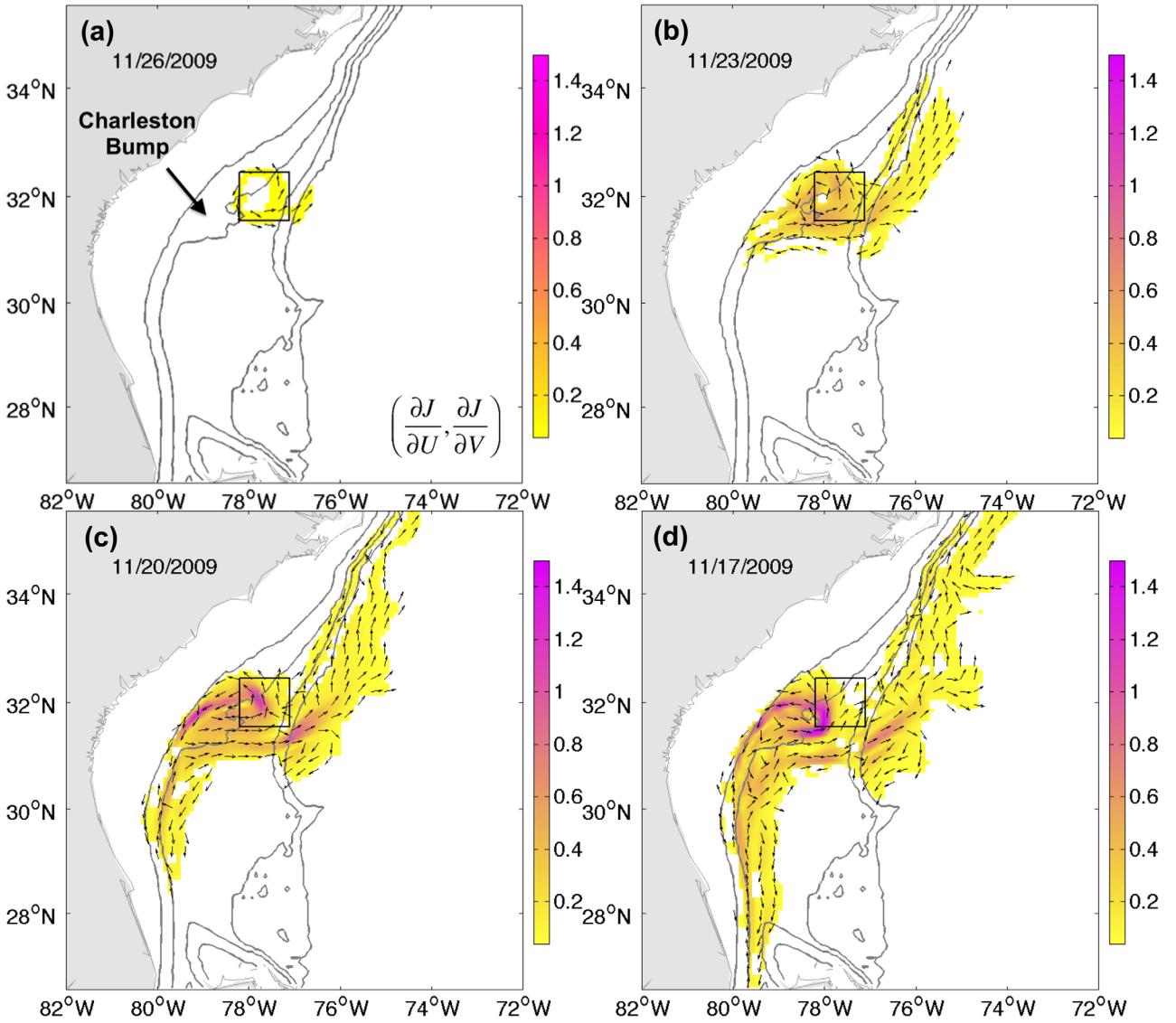

Figure 12. Adjoint sensitivity to depth-averaged velocity. Vectors represent direction. Color indicates magnitude (unit: 1/s). Gray lines are the 200, 600, 1000, and 2000 m isobaths. Black boxes are the region for index function calculation.

shoreward, and negative relative vorticity occurs seaward of the stream. An increased water transport would increase stream velocity while maintaining the shear balance (Figure 13b). However, the symmetric balance breaks down with the presence of the topographic Bump (Figure 13c). The blocking effect of the Bump leads to an enhancement of shoreward velocity shear and therefore an increase of the positive relative vorticity compared to those in the seaward. Therefore, a stream has an overall net increase of positive relative vorticity.

Now consider the first-order principle of potential vorticity (PV) conservation: $PV = \frac{f+\zeta}{h} = constant$, where f is the Coriolis parameter, ζ is relative vorticity, and h is water depth. Over the small geographic region being considered, f changes little. If net relative vorticity ζ associated with the flow increases, water depth h must increase in order to conserve potential vorticity. That implies that the stream must move further offshore to the deep water region. One caveat we note is that the diagnostic PV conservation equation applied here is the first-order approximation to the PV in the real, stratified ocean, where the baroclinic effect also contributes to the variation of vorticity [*Vallis*, 2006]. We adopt this first-order form to simplify of the mechanistic explanation. More quantitative vorticity term-by-term analysis is given in the next section.

4. Barotropic Vorticity Budget

To further verify the previous analysis, we calculated the barotropic vorticity budget in the SAB following *Marchesiello et al.* [2003] and *Gula et al.* [2015]. The full barotropic vorticity balance equation can be obtained by integrating the momentum equations in the vertical and cross differentiating them [*Gula et al.*, 2015]:

$$\underbrace{\frac{\partial \Omega}{\partial t}}_{\text{Tendency}} = \underbrace{-\nabla\cdot(f\bar{\mathbf{u}})}_{\text{BETA}} + \underbrace{\frac{\mathbf{J}(P_b,h)}{\rho_0}}_{\text{BPT}} + \underbrace{\mathbf{k}\cdot\nabla\times\frac{\boldsymbol{\tau}^{wind}}{\rho_0}}_{\text{WSC}} - \underbrace{\mathbf{k}\cdot\nabla\times\frac{\boldsymbol{\tau}^{bottom}}{\rho_0}}_{\text{BDC}} + \underbrace{D_\Sigma}_{\text{DIFF}} - \underbrace{A_\Sigma}_{\text{ADV}} \tag{11}$$

where the barotropic vorticity is defined as vorticity of the vertically integrated velocities $\Omega = \frac{\partial \bar{v}}{\partial x} - \frac{\partial \bar{u}}{\partial y}$ with $(u,\ v)$ as the $(x,\ y)$ components of the horizontal flow, the overbar denotes a vertically integrated quantity, $\mathbf{J}(P_b,h)$ is the Jacobian matrix of bottom pressure P_b and water depth h, τ is wind or bottom stress, and ρ_0 is the reference density. The terms on the r.h.s of equation (11) are planetary vorticity advection (BETA), bottom pressure torque (BPT), wind stress curl (WSC), bottom drag curl (BDC), horizontal diffusion (DIFF), and nonlinear advection (ADV). As a sanity check, the sum of BETA, BPT, and ADV nearly equals to the vorticity tendency term, within small numerical residual range (not shown).

Temporal mean values of dominant terms (tendency, BETA, BPT, and ADV) in equation (11) were calculated from 17 to 26 November 2009 (Figure 14). Along the path of the GS, large positive vorticity tendency occurred shoreward of the Charleston Bump and at the right bottom corner of the black box in Figure 14, which indicates an increase in barotropic vorticity. This is in agreement with the previous analysis that increased relative vorticity forces the GS move seaward due to conserving potential vorticity. Consistent with findings of previous studies in the same region [e.g., *Gula et al.*, 2015], the BETA, BPT and ADV terms are all quite noisy, especially around the region with rapid change of bathymetry. This is because equation (11) is obtained by vertically integrating and then cross differentiating the momentum equations. Both velocity derivatives and variation of bathymetry are noisy fields. Together they complicate the patterns and distributions of the resulting vorticity terms. Among them, the BPT term shows a positive contribution to the vorticity variation downstream of the Charleston Bump, indicating that the topography interacts with the velocity shear to provide a positive vorticity tendency. The ADV term, being another important term in the vorticity budget, provides a negative contribution to vorticity variation downstream of the Charleston Bump over the 10 day period.

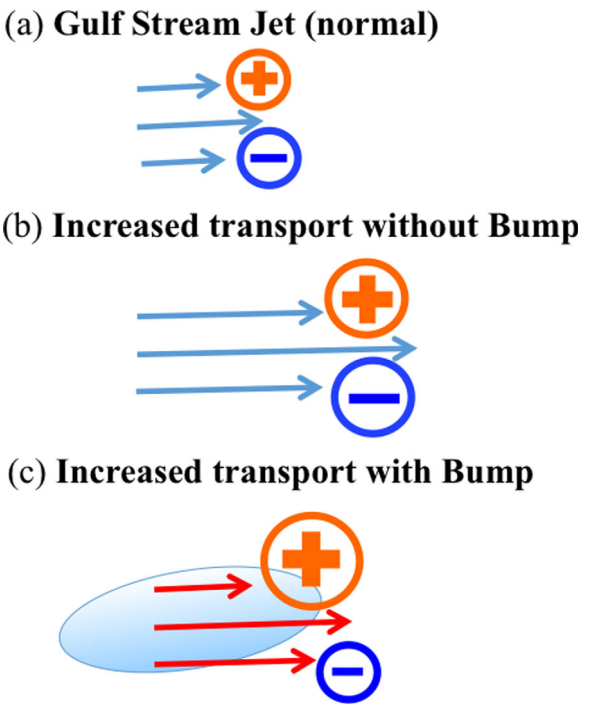

Figure 13. Schematics of positive relative vorticity perturbation formation. Orange circles with plus signs indicate positive relative vorticity. Blue circles with minus signs represent negative relative voracity. Vectors are velocity fields. Shaded ellipse represents the Charleston Bump.

To further explore the variation of different terms in equation (11), we calculated the spatial mean of each term in the area around the Charleston Bump (green box in Figure 14) from 17 to 26 November 2009 (Figure 15). The green box indicates the area that is important for the large GS offshore meander in this study. Similar to previous analyses, the dominant terms are the tendency, BETA, BPT, and ADV. Over the 10 days, the tendency term is mostly positive, which means the vorticity overall increases. Because the region is small, the BETA term changes little. The BPT term makes a positive contribution to the change of barotropic vorticity. But it is the ADV term that dominates the variation of the vorticity tendency term. The variation of the vorticity near the Charleston Bump during this time period generally corresponds to the increased water transport through the Florida

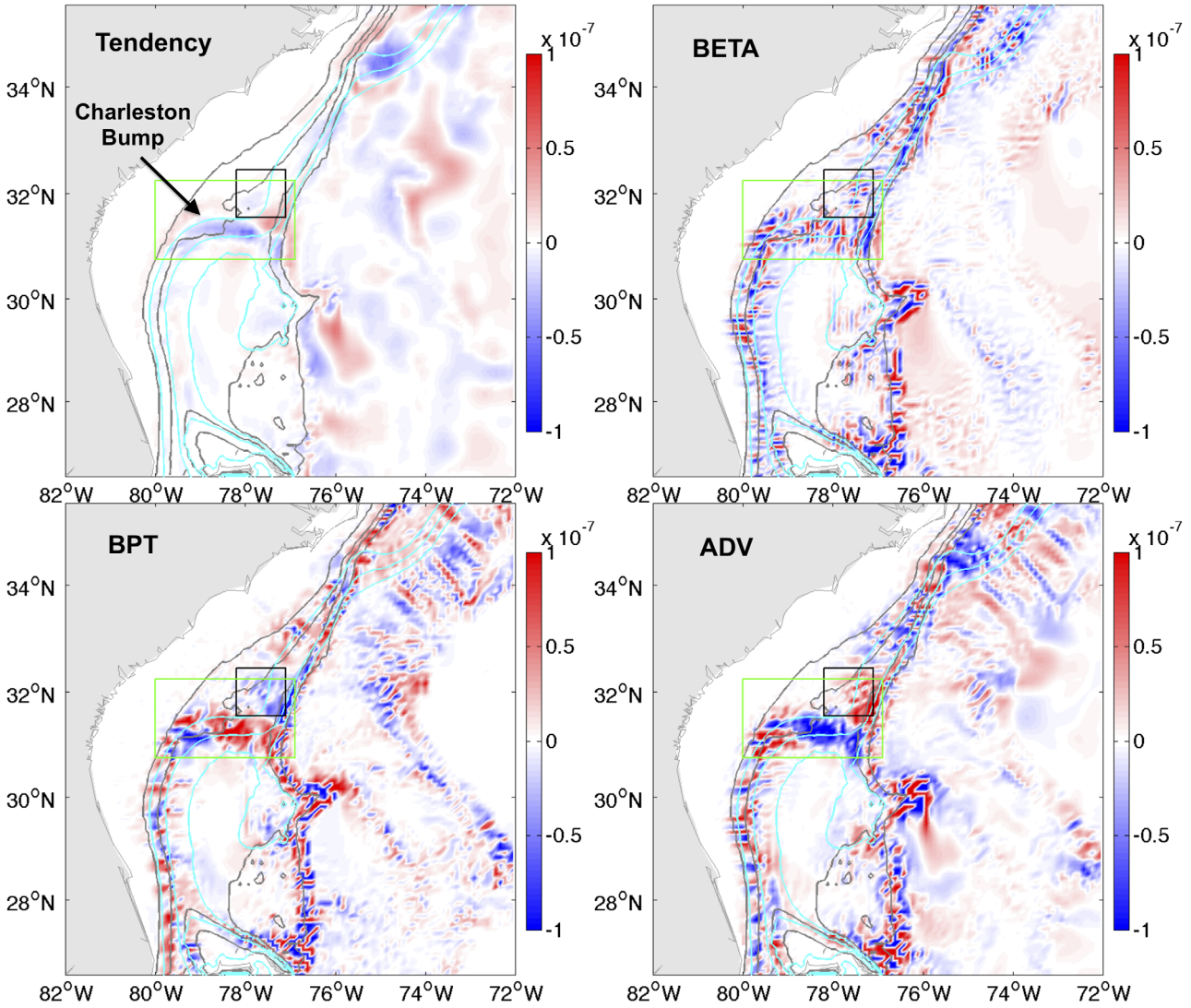

Figure 14. Ten day (17–26 November 2009) averaged tendency, planetary vorticity advection (BETA), bottom pressure torque (BPT), and nonlinear advection (ADV) terms in the barotropic vorticity equation (unit: m/s^2). Gray lines are the 200, 600, 1000, and 2000 m isobaths. Cyan lines are the 1, 21, and 41 Sv batrotropic streamlines (integrated from coastlines). Green boxes define the region for the time series plot in Figure 15. Black boxes indicate the region for the index function calculation.

Straits from 14 to 23 November (Figure 9). We also analyzed the energy balance following *Marchesiello et al.* [2003] and *Gula et al.* [2015]. Clearly there are significant energy transfers from potential energy to kinetic energy as well as from mean kinetic energy to eddy kinetic energy around the Charleston Bump during the study period (not shown). These findings are quite similar to the energetic analysis results of several previous studies [e.g., *Miller and Lee*, 1995; *Gula et al.*, 2015; *Kang and Curchitser*, 2015].

5. Summary

In this study, both the long-term and synoptic variability of the Gulf Stream path in the South Atlantic Bight and corresponding mechanisms are analyzed based on satellite altimetry observations, advanced numerical simulations, and vorticity budget analysis.

The Gulf Stream path was quantified using two decades of satellite altimeter data and the Self-Organizing Map (SOM). The variability of the Gulf Stream path generally increases from the Florida Straits to open ocean, supporting previous study by *Schmitz and McCartney* [1993]. Consistent with earlier study by *Bane and Dewar* [1988], the weakly and strongly deflected patterns of the Gulf Stream were also confirmed in our analysis. Overall,

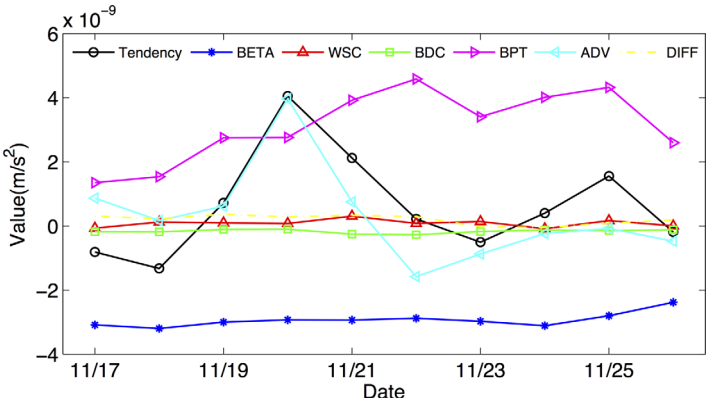

Figure 15. Spatial averaged terms of the barotropic vorticity equation (equation (11)) within the green box in Figure 14 (unit: m/s^2). The sign convention for the terms is exactly as indicated in equation (11), with tendency term on the l.h.s of the equation and the other terms on the r.h.s.

the weakly deflected pattern occurs more frequently than the strongly deflected pattern. As revealed by the SOM analysis, the strongly deflected pattern is more likely to occur in winter when the water transport through the Florida Straits is relatively low but with larger variability. This finding is consistent with *Miller*'s [1994] analysis about the Florida Current transport and the Gulf Stream path variation.

Over the last two decades, the largest Gulf Stream offshore meanders occurred in November 2009 to April 2010. We focused on the beginning stage (November 2009) of the extreme meander event. Triggering mechanisms of this Gulf Stream offshore meanders were explored using a regional implementation of ROMS forward model and its adjoint sensitivity analysis. The forward ocean model was skillful in reproducing the regional circulation in November 2009. By comparing water transport through three different transects (Figure 9), we found that the Gulf Stream transport upstream of the Charleston Bump was ~40 Sv in November 2009, among that ~75% (~30 Sv) originated from Florida Straits and ~25% (~10 Sv) came from the Antilles Current. A 10 day window (17–26 November 2009) was chosen for the backward in time adjoint sensitivity analysis based on the validity of tangent linear assumption. The sensitivity of Gulf Stream offshore meanders to the depth-averaged velocity field showed an increase of velocity in the Gulf Stream, which interacted with the local topography near the Charleston Bump to generate an asymmetric velocity shear. As a result, there was a net increase of positive relative vorticity, indicated by the cyclonic velocity perturbation around the Bump (Figure 11). The increased relative vorticity forced the Gulf Stream to move further offshore to conserve potential vorticity. The adjoint sensitivity analysis showed this process corresponded to a Florida current transport increase starting from 15 November 2009.

Barotropic vorticity budget analysis further confirmed these findings. The dominant terms in the barotropic vorticity budget are the planetary vorticity advection, bottom pressure torque, and the nonlinear advection. During the study time period, the vorticity tendency near the Charleston Bump, mostly remains positive, indicating an overall increase in relative vorticity. Its variation is mostly dominated by the nonlinear advection. This study focuses on the triggering mechanism of the Gulf Stream offshore deflection in November 2009. What allowed the offshore deflection to maintain afterward for several months is a unique offshore forcing condition that worked in concert. We will report this maintaining mechanism in a future correspondence.

Acknowledgments
The authors thank A. M. Moore from University of California, Santa Cruz, J. Bane and H. Seim of University of North Carolina, Chapel Hill, B. Powell from University of Hawaii, Manoa, and W. G. Zhang and Y. Li from Woods Hole Oceanographic Institution for their helpful discussions of this study. Research support provided by NSF grants: OCE 1029841 and OCE1559178; NOAA grants: NA11NOS0120033 and NA14NMF4540061; NASA grants: NNX12AP84G, NNX13AD80G, and NNX14AO73G are greatly appreciated. We also thank two anonymous reviewers for their valuable comments. The AVISO altimeter data used in the analysis are available at: http://www.aviso.altimetry.fr/en/home.html and the Florida current volume transport data are available at: http://www.aoml.noaa.gov/phod/floridacurrent/data_access.php.

References

Bane, J. M., and W. K. Dewar (1988), Gulf Stream bimodality and variability downstream of the Charleston bump, *J. Geophys. Res.*, *93*(C6), 6695–6710, doi:10.1029/JC093iC06p06695.

Bane, J. M., and K. E. Osgood (1989), Wintertime air-sea interaction processes across the Gulf Stream, *J. Geophys. Res.*, *94*(C8), 10,755–10,772, doi:10.1029/JC094iC08p10755.

Bertsekas, D. P. (1982), *Constrained optimization and Lagrange multiplier methods*, Computer science and applied mathematics, Academic Press, N. Y.

Bennett, A. F. (1992), *Inverse Methods in Physical Oceanography*, Cambridge Univ. Press, Cambridge, U. K.

Bennett, A. F. (2002), *Inverse Modeling of the Ocean and Atmosphere*, Cambridge Univ. Press, Cambridge, U. K.

Broquet, G., C. A. Edwards, A. M. Moore, B. S. Powell, M. Veneziani, and J. D. Doyle (2009), Application of 4D-Variational data assimilation to the California Current System, *Dyn. Atmos. Oceans*, *48*(1–3), 69–92, doi:10.1016/j.dynatmoce.2009.03.001.

Bugnion, V., C. Hill, and P. H. Stone (2006), An adjoint analysis of the meridional overturning circulation in an ocean model, *J. Clim.*, *19*(15), 3732–3750, doi:10.1175/JCLI3787.1.

Canny, J. (1986), A computational approach to edge detection, *IEEE Trans. Pattern Anal. Mach. Intell.*, *8*(6), 679–698, doi:10.1109/TPAMI.1986.4767851.

Castelao, R. (2011), Intrusions of Gulf Stream waters onto the South Atlantic Bight shelf, *J. Geophys. Res.*, *116*, C10011, doi:10.1029/2011JC007178.

Chelton, D. B., M. G. Schlax, and R. M. Samelson (2011), Global observations of nonlinear mesoscale eddies, *Prog. Oceanogr.*, *91*(2), 167–216, doi:10.1016/j.pocean.2011.01.002.

Chua, B. S., and A. F. Bennett (2001), An inverse ocean modeling system, *Ocean Modell.*, *3*(3–4), 137–165, doi:10.1016/S1463-5003(01)00006-3.

Epifanio, C. E., and R. W. Garvine (2001), Larval transport on the Atlantic Continental Shelf of North America: A review, *Estuarine Coastal Shelf Sci.*, *52*(1), 51–77, doi:10.1006/ecss.2000.0727.

Errico, R. M. (1997), What is an adjoint model?, *Bull. Am. Meteorol. Soc.*, *78*(11), 2577–2591, doi:10.1175/1520-0477(1997)078 < 2577:WIAAM>2.0.CO;2.

Ezer, T. (2015), Detecting changes in the transport of the Gulf Stream and the Atlantic overturning circulation from coastal sea level data: The extreme decline in 2009–2010 and estimated variations for 1935–2012, *Global Planet. Change*, *129*, 23–36, doi:10.1016/j.gloplacha.2015.03.002.

Fairall, C. W., E. F. Bradley, D. P. Rogers, J. B. Edson, and G. S. Young (1996), Bulk parameterization of air-sea fluxes for Tropical Ocean-Global Atmosphere Coupled-Ocean Atmosphere Response Experiment, *J. Geophys. Res.*, *101*(C2), 3747–3764, doi:10.1029/95JC03205.

Frankignoul, C., G. de Coëtlogon, T. M. Joyce, and S. Dong (2001), Gulf stream variability and ocean–atmosphere interactions, *J. Phys. Oceanogr.*, *31*(12), 3516–3529.

Goddard, P. B., J. Yin, S. M. Griffies, and S. Zhang (2015), An extreme event of sea-level rise along the Northeast coast of North America in 2009–2010, *Nat. Commun.*, *6*, doi:10.1038/ncomms7346.

Gopalakrishnan, G., B. D. Cornuelle, and I. Hoteit (2013), Adjoint sensitivity studies of loop current and eddy shedding in the Gulf of Mexico, *J. Geophys. Res. Atmos. Oceans*, *118*, 3315–3335, doi:10.1002/jgrc.20240.

Gula, J., M. J. Molemaker, and J. C. McWilliams (2015), Gulf Stream dynamics along the southeastern U.S. seaboard, *J. Phys. Oceanogr.*, *45*(3), 690–715, doi:10.1175/JPO-D-14-0154.1.

Gunn, J. T., and D. R. Watts (1982), On the currents and water masses north of the Antilles/Bahamas Arc, *J. Mar. Res.*, *40*, 1–48.

Haidvogel, D. B., et al. (2008), Ocean forecasting in terrain-following coordinates: Formulation and skill assessment of the Regional Ocean Modeling System, *J. Comput. Phys.*, *227*(7), 3595–3624, doi:10.1016/j.jcp.2007.06.016.

Ishikawa, Y., T. Awaji, N. Komori, and T. Toyoda (2004), Application of sensitivity analysis using an adjoint model for short-range forecasts of the Kuroshio path south of Japan, *J. Oceanogr.*, *60*(2), 293–301, doi:10.1023/B:JOCE.0000038335.50080.ff.

Ito, K., and K. Kunisch (2008), *Lagrange multiplier approach to variational problems and applications*, Advances in design and control; 15, Society for Industrial and Applied Mathematics, Pa.

Jin, B., G. Wang, Y. Liu, and R. Zhang (2010), Interaction between the East China Sea Kuroshio and the Ryukyu Current as revealed by the self-organizing map, *J. Geophys. Res. Atmos.*, *115*, C12047, doi:10.1029/2010JC006437.

Joyce, T. M., and R. Zhang (2010), On the path of the Gulf Stream and the Atlantic Meridional Overturning Circulation, *J. Clim.*, *23*(11), 3146–3154, doi:10.1175/2010JCLI3310.1.

Joyce, T. M., C. Deser, and M. A. Spall (2000), The relation between decadal variability of subtropical mode water and the North Atlantic Oscillation*, *J. Clim.*, *13*(14), 2550–2569, doi:10.1175/1520-0442(2000)013 < 2550:TRBDVO>2.0.CO;2.

Joyce, T. M., Y.-O. Kwon, and L. Yu (2009), On the relationship between synoptic wintertime atmospheric variability and path shifts in the Gulf Stream and the Kuroshio extension, *J. Clim.*, *22*(12), 3177–3192, doi:10.1175/2008JCLI2690.1.

Kang, D., and E. N. Curchitser (2015), Energetics of eddy–mean flow interactions in the Gulf Stream region, *J. Phys. Oceanogr.*, *45*(4), 1103–1120, doi:10.1175/JPO-D-14-0200.1.

Kohonen, T. (2001), *Self-Organizing Maps, Springer Ser. Inf. Sci.*, Springer, Berlin.

Kwon, Y.-O., M. A. Alexander, N. A. Bond, C. Frankignoul, H. Nakamura, B. Qiu, and L. A. Thompson (2010), Role of the Gulf Stream and Kuroshio–Oyashio systems in large-scale atmosphere–ocean interaction: A review, *J. Clim.*, *23*(12), 3249–3281, doi:10.1175/2010JCLI3343.1.

Lee, T. N., J. A. Yoder, and L. P. Atkinson (1991), Gulf Stream frontal eddy influence on productivity of the southeast U.S. continental shelf, *J. Geophys. Res.*, *96*(C12), 22,191–22,205, doi:10.1029/91JC02450.

Lee, T. N., W. E. Johns, R. J. Zantopp, and E. R. Fillenbaum (1996), Moored observations of Western Boundary Current variability and thermohaline circulation at 26.5° in the subtropical North Atlantic, *J. Phys. Oceanogr.*, *26*(6), 962–983, doi:10.1175/1520-0485(1996)026 < 0962:MOOWBC>2.0.CO;2.

Li, Y., H. Xue, and J. M. Bane (2002), Air-sea interactions during the passage of a winter storm over the Gulf Stream: A three-dimensional coupled atmosphere-ocean model study, *J. Geophys. Res.*, *107*(C11), 3200, doi:10.1029/2001JC001161.

Lillibridge, J. L., III, and A. J. Mariano (2013), A statistical analysis of Gulf Stream variability from 18+ years of altimeter data, *Deep Sea Res., Part II*, *85*, 127–146, doi:10.1016/j.dsr2.2012.07.034.

Liu, Y., and R. H. Weisberg (2005), Patterns of ocean current variability on the West Florida Shelf using the self-organizing map, *J. Geophys. Res. Atmos.*, *110*, C06003, doi:10.1029/2004JC002786.

Liu, Y., R. H. Weisberg, and C. N. K. Mooers (2006a), Performance evaluation of the self-organizing map for feature extraction, *J. Geophys. Res. Atmos.*, *111*, C05018, doi:10.1029/2005JC003117.

Liu, Y., R. H. Weisberg, and R. He (2006b), Sea surface temperature patterns on the West Florida shelf using growing hierarchical self-organizing maps, *J. Atmos. Oceanic Technol.*, *23*(2), 325–338, doi:10.1175/JTECH1848.1.

Liu, Y., R. H. Weisberg, and L. K. Shay (2007), Current patterns on the West Florida shelf from joint self-organizing map analyses of HF radar and ADCP data, *J. Atmos. Oceanic Technol.*, *24*(4), 702–712, doi:10.1175/JTECH1999.1.

Liu, Y., R. H. Weisberg, and Y. Yuan (2008), Patterns of upper layer circulation variability in the South China Sea from satellite altimeter using the Self-Organizing Map, *Acta Oceanol. Sin.*, *27*, 129–144.

Liu, Z., and J. Gan (2012), Variability of the Kuroshio in the East China Sea derived from satellite altimeter data, *Deep Sea Res., Part I*, *59*, 25–36, doi:10.1016/j.dsr.2011.10.008.

Marchesiello, P., J. C. McWilliams, and A. Shchepetkin (2001), Open boundary conditions for long-term integration of regional oceanic models, *Ocean Modell.*, *3*(1–2), 1–20, doi:10.1016/S1463-5003(00)00013-5.

Marchesiello, P., J. C. McWilliams, and A. Shchepetkin (2003), Equilibrium structure and dynamics of the California current system, *J. Phys. Oceanogr.*, *33*(4), 753–783, doi:10.1175/1520-0485(2003)33 < 753:ESADOT>2.0.CO;2.

Marotzke, J., R. Giering, K. Q. Zhang, D. Stammer, C. Hill, and T. Lee (1999), Construction of the adjoint MIT ocean general circulation model and application to Atlantic heat transport sensitivity, *J. Geophys. Res.*, *104*(C12), 29,529–29,547, doi:10.1029/1999JC900236.

Miller, J. L. (1994), Fluctuations of Gulf Stream frontal position between Cape Hatteras and the Straits of Florida, *J. Geophys. Res.*, *99*(C3), 5057–5064, doi:10.1029/93JC03484.

Miller, J. L., and T. N. Lee (1995), Gulf Stream meanders in the South Atlantic Bight: 1. Scaling and energetics, *J. Geophys. Res.*, *100*(C4), 6687–6704, doi:10.1029/94JC02542.

Minobe, S., M. Miyashita, A. Kuwano-Yoshida, H. Tokinaga, and S.-P. Xie (2010), Atmospheric response to the Gulf Stream: Seasonal variations, *J. Clim.*, *23*(13), 3699–3719, doi:10.1175/2010JCLI3359.1.

Moore, A. M., H. G. Arango, E. Di Lorenzo, B. D. Cornuelle, A. J. Miller, and D. J. Neilson (2004), A comprehensive ocean prediction and analysis system based on the tangent linear and adjoint of a regional ocean model, *Ocean Modell.*, *7*(1–2), 227–258, doi:10.1016/j.ocemod.2003.11.001.

Moore, A. M., H. G. Arango, E. Di Lorenzo, A. J. Miller, and B. D. Cornuelle (2009), An adjoint sensitivity analysis of the southern California current circulation and ecosystem, *J. Phys. Oceanogr.*, *39*(3), 702–720, doi:10.1175/2008JPO3740.1.

Moore, A. M., H. G. Arango, G. Broquet, C. Edwards, M. Veneziani, B. Powell, D. Foley, J. D. Doyle, D. Costa, and P. Robinson (2011a), The Regional Ocean Modeling System (ROMS) 4-dimensional variational data assimilation systems: Part III—Observation impact and observation sensitivity in the California Current System, *Prog. Oceanogr.*, *91*(1), 74–94, doi:10.1016/j.pocean.2011.05.005.

Moore, A. M., H. G. Arango, G. Broquet, C. Edwards, M. Veneziani, B. Powell, D. Foley, J. D. Doyle, D. Costa, and P. Robinson (2011b), The Regional Ocean Modeling System (ROMS) 4-dimensional variational data assimilation systems: Part II—Performance and application to the California Current System, *Prog. Oceanogr.*, *91*(1), 50–73, doi:10.1016/j.pocean.2011.05.003.

Moore, A. M., H. G. Arango, G. Broquet, B. S. Powell, A. T. Weaver, and J. Zavala-Garay (2011c), The Regional Ocean Modeling System (ROMS) 4-dimensional variational data assimilation systems: Part I—System overview and formulation, *Prog. Oceanogr.*, *91*(1), 34–49, doi:10.1016/j.pocean.2011.05.004.

Mujumdar, P. P., and D. N. Kumar (2012), *Floods in a Changing Climate, Hydrologic Modeling, International Hydrology Series*, Cambridge University Press, Cambridge, U. K.

Nelson, J., and R. He (2012), Effect of the Gulf Stream on winter extratropical cyclone outbreaks, *Atmos. Sci. Lett.*, *13*(4), 311–316, doi:10.1002/asl.400.

Nelson, J., R. He, J. C. Warner, and J. Bane (2014), Air–sea interactions during strong winter extratropical storms, *Ocean Dyn.*, *64*(9), 1233–1246, doi:10.1007/s10236-014-0745-2.

Peña-Molino, B., and T. M. Joyce (2008), Variability in the slope water and its relation to the Gulf Stream path, *Geophys. Res. Lett.*, *35*, L03606, doi:10.1029/2007GL032183.

Pérez-Hernández, M. D., and T. M. Joyce (2014), Two modes of Gulf Stream variability revealed in the last two decades of satellite altimeter data, *J. Phys. Oceanogr.*, *44*(1), 149–163, doi:10.1175/JPO-D-13-0136.1.

Powell, B. S., H. G. Arango, A. M. Moore, E. Di Lorenzo, R. F. Milliff, and D. Foley (2008), 4DVAR data assimilation in the Intra-Americas Sea with the Regional Ocean Modeling System (ROMS), *Ocean Modell.*, *23*(3–4), 130–145, doi:10.1016/j.ocemod.2008.04.008.

Reusch, D. B., R. B. Alley, and B. C. Hewitson (2007), North Atlantic climate variability from a self-organizing map perspective, *J. Geophys. Res. Atmos.*, *112*, D02104, doi:10.1029/2006JD007460.

Rowe, E., A. J. Mariano, and E. H. Ryan (2013), The Antilles Current, University of Miami, Fla. [Available at http://oceancurrents.rsmas.miami.edu/atlantic/antilles.html.]

Sanchez-Franks, A., and R. Zhang (2015), Impact of the Atlantic Meridional Overturning Circulation on the decadal variability of the Gulf Stream path and regional chlorophyll and nutrient concentrations, *Geophys. Res. Lett.*, *42*, 9889–9887, doi:10.1002/2015GL066262.

Schmeits, M. J., and H. A. Dijkstra (2001), Bimodal behavior of the Kuroshio and the Gulf Stream, *J. Phys. Oceanogr.*, *31*(12), 3435–3456, doi:10.1175/1520-0485(2001)031 < 3435:BBOTKA>2.0.CO;2.

Schmitz, W. J., and M. S. McCartney (1993), On the North Atlantic Circulation, *Rev. Geophys.*, *31*(1), 29–49, doi:10.1029/92RG02583.

Shchepetkin, A. F., and J. C. McWilliams (2005), The regional oceanic modeling system (ROMS): A split-explicit, free-surface, topography-following-coordinate oceanic model, *Ocean Modell.*, *9*(4), 347–404, doi:10.1016/j.ocemod.2004.08.002.

Signorini, S. R., and C. R. McClain (2007), Large-scale forcing impact on biomass variability in the South Atlantic Bight, *Geophys. Res. Lett.*, *34*, L21605, doi:10.1029/2007GL031121.

Sikirić, M. D., I. Janeković, and M. Kuzmić (2009), A new approach to bathymetry smoothing in sigma-coordinate ocean models, *Ocean Modell.*, *29*(2), 128–136, doi:10.1016/j.ocemod.2009.03.009.

Solidoro, C., V. Bandelj, P. Barbieri, G. Cossarini, and S. Fonda Umani (2007), Understanding dynamic of biogeochemical properties in the northern Adriatic Sea by using self-organizing maps and k-means clustering, *J. Geophys. Res.*, *112*, C07S90, doi:10.1029/2006JC003553.

Srokosz, M. A., and H. L. Bryden (2015), Observing the Atlantic Meridional Overturning Circulation yields a decade of inevitable surprises, *Science*, *348*(6241), 1255575, doi:10.1126/science.1255575.

SSALTO/DUACS User Handbook (2015), *SSALTO/DUACS User Handbook: (M)SLA and (M)ADT Near-Real Time and Delayed Time Products*, CNES, Toulouse, France.

Tsui, I.-F., and C.-R. Wu (2012), Variability analysis of Kuroshio intrusion through Luzon Strait using growing hierarchical self-organizing map, *Ocean Dyn.*, *62*(8), 1187–1194, doi:10.1007/s10236-012-0558-0.

Vallis, G. K. (2006), *Atmospheric and Oceanic Fluid Dynamics: Fundamentals and Large-Scale Circulation*, pp. 178–188, Cambridge Univ. Press, Cambridge, U. K.

Veneziani, M., C. A. Edwards, and A. M. Moore (2009), A central California coastal ocean modeling study: 2. Adjoint sensitivities to local and remote forcing mechanisms, *J. Geophys. Res.*, *114*(C4), C04020, doi:10.1029/2008JC004775.

Warner, J. C., C. R. Sherwood, H. G. Arango, and R. P. Signell (2005), Performance of four turbulence closure models implemented using a generic length scale method, *Ocean Modell.*, *8*(1–2), 81–113, doi:10.1016/j.ocemod.2003.12.003.

Webster, F. (1961), A description of gulf stream meanders off Onslow Bay, *Deep Sea Res.*, *8*(2), 130–143, doi:10.1016/0146-6313(61)90005-3.

Werner, F. E., J. A. Quinlan, B. O. Blanton, and R. A. Luettich Jr. (1997), The role of hydrodynamics in explaining variability in fish populations, *J. Sea Res.*, *37*(3–4), 195–212, doi:10.1016/S1385-1101(97)00024-5.

Wunsch, C. (1996), *The Ocean Circulation Inverse Problem*, Cambridge Univ. Press, Cambridge, U. K.

Wunsch, C. (2006), *Discrete Inverse and State Estimation Problems: With Geophysical Fluid Applications*, Cambridge Univ. Press, Cambridge, U. K.

Xie, L., X. Liu, and L. J. Pietrafesa (2007), Effect of bathymetric curvature on Gulf Stream instability in the vicinity of the Charleston Bump, *J. Phys. Oceanogr.*, *37*(3), 452–475, doi:10.1175/JPO2995.1.

Yin, Y., X. Lin, Y. Li, and X. Zeng (2014), Seasonal variability of Kuroshio intrusion northeast of Taiwan Island as revealed by self-organizing map, *Chin. J. Oceanol. Limnol.*, *32*(6), 1435–1442, doi:10.1007/s00343-015-4017-x.

Zhang, W. G., J. L. Wilkin, J. C. Levin, and H. G. Arango (2009), An Adjoint Sensitivity Study of Buoyancy- and Wind-Driven Circulation on the New Jersey Inner Shelf, *J. Phys. Oceanogr.*, *39*(7), 1652–1668, doi:10.1175/2009JPO4050.1.

Zeng, X., Y. Li, R. He, and Y. Yin (2015a), Clustering of Loop Current patterns based on the satellite-observed sea surface height and self-organizing map, *Remote Sens. Lett.*, *6*(1), 11–19, doi:10.1080/2150704X.2014.998347.

Zeng, X., Y. Li, and R. He (2015b), Predictability of the loop current variation and eddy shedding process in the Gulf of Mexico using an artificial neural network approach, *J. Atmos. Oceanic Technol.*, *32*(5), 1098–1111, doi:10.1175/JTECH-D-14-00176.1.